Total reaction cross section σ_{reac} of α-induced reactions from elastic scattering: The example ^{140}Ce(α,α)^{140}Ce

Peter Mohr[*]

Diakonie-Klinikum, D-74523 Schwäbisch Hall, Germany and Institute of Nuclear Research (ATOMKI), H-4001 Debrecen, Hungary

Angular distributions of elastic ^{140}Ce(α,α)^{140}Ce scattering are analyzed in the framework of the optical model from low energies around the Coulomb barrier up to about 40 MeV. From the local fits the total reaction cross section σ_{reac} is extracted. This procedure requires experimental scattering data with small uncertainties. The results for σ_{reac} are compared to predictions of different systematic global potentials. It is found that the total reaction cross section σ_{reac} is well predicted from all global potentials under study although the reproduction of the angular distributions is not perfect in all cases. In addition, the lower energy limit for the extraction of σ_{reac} from elastic scattering angular distributions is analyzed. Finally, the potentials under study are used to calculate the ^{143}Nd(n,α)^{140}Ce cross section, and the predictions are compared to experimental data.

I. INTRODUCTION

The total reaction cross section σ_{reac} is a basic quantity for the prediction of reaction cross sections in the statistical model. It has been found that especially at low energies huge discrepancies are found between predictions for α-induced reaction cross sections using different global α-nucleus optical potentials. This holds in particular for (α,γ) capture reactions for targets with masses above $A \approx 100$ [1–8], but also the energy dependence of recent (α,n) data for ^{141}Pr was difficult to fit [9,10].

The total reaction cross section σ_{reac} is related to the complex scattering matrix $S_L = \eta_L \exp{(2i\delta_L)}$ by the well-known relation

$$\sigma_{\mathrm{reac}} = \sum_L \sigma_L = \frac{\pi}{k^2} \sum_L (2L+1)\left(1 - \eta_L^2\right), \quad (1)$$

where $k = \sqrt{2\mu E_{\mathrm{c.m.}}}/\hbar$ is the wave number, $E_{\mathrm{c.m.}}$ is the energy in the center-of-mass (c.m.) system, and η_L and δ_L are the real reflexion coefficients and scattering phase shifts. σ_L is the contribution of the Lth partial wave to the total reaction cross section σ_{reac}. The relation in Eq. (1) has recently been confirmed experimentally at low energies [11].

The present study determines σ_{reac} from the angular distributions at $E_{\mathrm{lab}} = 14.7$ MeV [12] and 19.0, 24.0, 32.0, and 37.7 MeV [13]. The latter data are unfortunately not published. The data have been measured at the XTU Tandem of the INFN Laboratori Nazionali di Legnaro using a cerium target enriched to about 96% in the semimagic $N = 82$ nucleus ^{140}Ce. Access to the numerical ^{140}Ce(α,α)^{140}Ce scattering data of [13] will be provided via the EXFOR database [14]. In addition, elastic scattering data for natural cerium (^{140}Ce: 88.48%) are available in literature [15]. These data have also been analyzed, and the results fit into the observed systematics of total reaction cross sections. However, the angular distributions are not shown here because they may be affected by the other cerium isotopes.

The obtained results for σ_{reac} are compared to predictions from recently published α-nucleus potentials [16–18] and to the widely used potential by McFadden and Satchler [19]. The example of ^{140}Ce is well suited for a study of uncertainties for σ_{reac} at low energies because experimental scattering data are available down to relatively low energies. Further information on the α-nucleus potential can be derived from reaction data at very low energies. Often the (α,n) reaction has been used for this purpose (see, e.g., [9,10]), but in the present case there are no experimental data for the ^{140}Ce(α,n)^{143}Nd reaction. Instead, the reverse ^{143}Nd(n,α)^{140}Ce reaction will be investigated here.

II. OPTICAL MODEL ANALYSIS

The elastic scattering angular distributions are analyzed in the usual way within the framework of the optical model and a complex α-nucleus optical potential. Details of the fitting procedure for this local fit are similar to Refs. [10,18] and are only briefly summarized here.

The total potential $U(r)$ is composed of the real Coulomb potential $V_C(r)$ and the complex nuclear potential $V(r) + iW(r)$. The Coulomb potential is calculated from a homogenously charged sphere where the Coulomb radius is taken from the root-mean-square (rms) radius of the real folding potential (see below). Properties of the real and imaginary part of the nuclear potential are presented in the next paragraphs.

A. Real part of the nuclear potential

The real part of the nuclear potential is determined by a double-folding procedure where the folding potential $V_F(r)$ is modified by a strength parameter λ and a width parameter w:

$$V(r) = \lambda \, V_F(r/w). \quad (2)$$

The strength parameter λ and the width parameter w will be adjusted to the experimental ^{140}Ce(α,α)^{140}Ce angular distributions. Obviously, the width parameter w should remain close to unity; otherwise, the folding potential would be questionable. The strength parameter λ is typically around

_____

[*]widmaiermohr@t-online.de

TABLE I. Experimental charge density distribution of ^{140}Ce as listed in Table A.1 of [24], parametrized by a Fourier-Bessel series: $\rho(r) = \sum_n G_n \times j_0(n\pi r/R_{FB})$ with the Fourier-Bessel cutoff radius $R_{FB} = 10$ fm.

n	G_n	n	G_n
1	0.759956	2	0.578531
3	−0.589376	4	−0.184926
5	0.337939	6	0.006674
7	−0.132665	8	0.002477
9	0.002589	10	−0.013456

1.1 to 1.4 leading to volume integrals per interacting nucleon pair of $J_R \approx 310$–350 MeV fm^3 [20]. (As usual, the negative signs of J_R and J_I are neglected in the following discussion.)

The calculation of the folding potential requires the density of the ^{140}Ce target nucleus which is usually derived from electron scattering. Although no data are available in the widely used compilation [21], two papers [22,23] use a ^{140}Ce density and refer to a "complementary, high-precision, elastic electron scattering experiment performed at Saclay" with the reference "D. Goutte *et al.*, to be published". The density parameters in Fourier-Bessel parametrization can be found in an underlying Ph.D. thesis by Miller [24], Table A.1, and are repeated here for easier access in future work (see Table I). The resulting folding potential is very close to the average of the potentials for the neighboring $N = 82$ nuclei ^{139}La and ^{142}Nd; thus, the reliability of the unpublished electron density of ^{140}Ce from [24] is confirmed.

B. Imaginary part of the nuclear potential

The imaginary part of the optical potential is parametrized by the usual Woods-Saxon (WS) potentials of volume and surface type. Except at the higher energies under study where an additional volume Woods-Saxon potential is required, only a surface Woods-Saxon potential was used:

$$W(r) = W_V f(x_V) + W_S \frac{df(x_S)}{dx_S}. \quad (3)$$

W_i are the depth parameters of the volume and surface imaginary potential, and the Woods-Saxon function $f(x_i)$ is

given by

$$f(x_i) = [1 + \exp(x_i)]^{-1} \quad (4)$$

with $x_i = (r - R_i A_T^{1/3})/a_i$ and $i = V, S$ for the volume and surface part. Note that $W_V < 0$ and $W_S > 0$ in the chosen conventions (3) and (4) for an absorptive negative $W(r) < 0$. The maximum depth of the surface imaginary potential is given by $-W_S/4$ at $r = R_S A_T^{1/3}$.

C. Results

The parameters of the nuclear potential are adjusted to the experimental angular distributions using a standard χ^2 minimizing procedure. The resulting parameters are listed in Table II, and the fits are compared to the experimental angular distributions in Fig. 1. Excellent agreement between the local fits and the experimental data is obtained at all energies under study. For the real part the parameters of the fits show very minor variations with energy and are in their expected ranges [20]. The parameters of the real and imaginary parts of the potential will be discussed in detail below.

The width parameter w is about 1.5% larger than unity and practically constant except at the highest energy for ^{140}Ce. The strength parameter λ varies by about 10% between 1.15 and 1.28; this leads to a similar variation of the real volume integral J_R which shows a maximum of 341 MeV fm^3 at 24 MeV and slightly smaller values at higher and lower energies (similar to the finding in [25]). The variation of the potential parameters of the real part is relatively small, and thus the real part of the potential and its energy dependence should not be the reason for major uncertainties in the prediction of α-induced reaction cross sections at low energies.

Contrary to the real part, the imaginary part shows a significant energy dependence. The most obvious signature is the change from a surface Woods-Saxon potential at very low energies to a dominating volume Woods-Saxon potential at the higher energies under study. It is sufficient to use a pure surface Woods-Saxon potential at the lower energies below 25 MeV, and reduced χ^2/F values around unity are obtained. The variation of the geometry of the surface imaginary part at the lower energies is small: the radius parameter R_S varies by less than 5% around its average value, and the diffuseness a_S shows a somewhat larger spread of about 25% around its

TABLE II. Parameters of the optical potential and the total reaction cross section σ_{reac} derived from ^{140}Ce$(\alpha,\alpha)^{140}$Ce angular distributions.

E_{lab} (MeV)	$E_{\text{c.m.}}$ (MeV)	λ (−)	w (−)	J_R (MeV fm^3)	$r_{R,\text{rms}}$ (fm)	W_V (MeV)	R_V (fm)	a_V (fm)	W_S (MeV)	R_S (fm)	a_S (fm)	J_I (MeV fm^3)	$r_{I,\text{rms}}$ (fm)	χ^2/F (−)	σ_{reac}[a] (mb)	Ref. Exp.
14.69	14.28	1.146	1.021	315.8	5.641			−	28.0	1.444	0.507	18.2	7.774	0.1	28 ± 4	[12]
19.0	18.47	1.218	1.014	328.1	5.599			−	101.8	1.517	0.303	43.1	7.970	0.7	399 ± 30	[13]
23.97	23.30	1.253	1.017	340.7	5.616			−	114.0	1.445	0.434	63.2	7.709	0.8	999 ± 30	[13]
32.0	31.11	1.276	1.006	336.0	5.557	−21.1	1.311	0.211	13.4	1.574	0.416	58.6	5.860	0.8	1453 ± 44	[13]
37.7	36.65	1.265	0.999	326.3	5.518	−19.1	1.374	0.269	8.9	1.580	0.729	62.6	6.218	1.0	1824 ± 55	[13]
45.0[b]	43.75	1.195	1.020	328.3	5.635	−28.2	1.028	0.809	28.0	1.516	0.504	59.3	6.291	0.4	1940 ± 97[c]	[15]

[a]From the local potential fit using Eq. (1); uncertainties estimated from the model-independent phase shift analysis.
[b]Natural cerium (^{140}Ce: 88.48%).
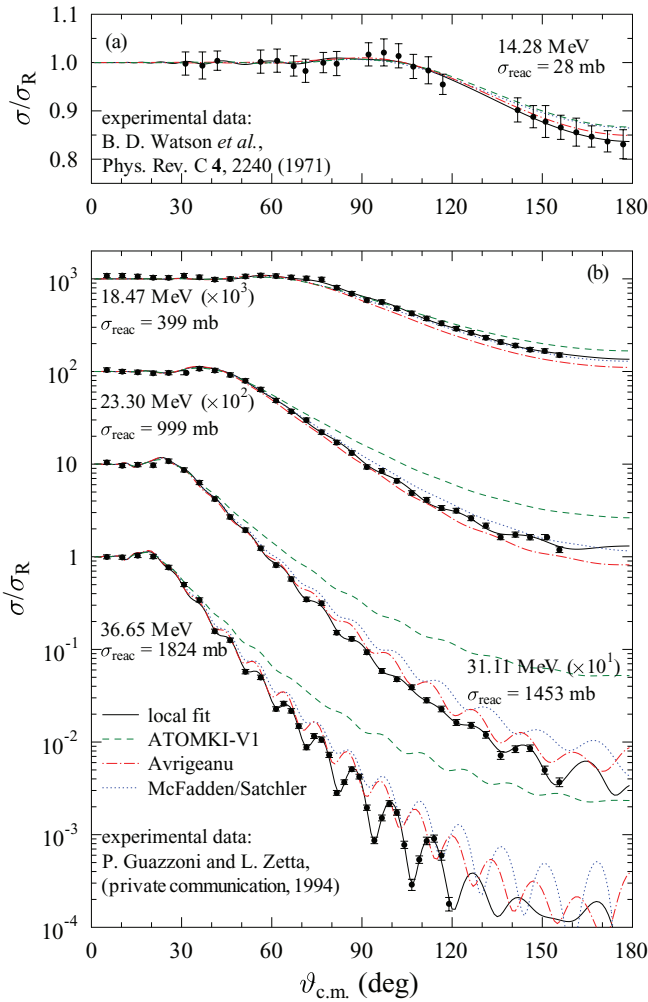[c]Increased 5% uncertainty because of contributions from other cerium isotopes.

FIG. 1. (Color online) Rutherford normalized elastic scattering cross sections of the ^{140}Ce$(\alpha,\alpha)^{140}$Ce reaction versus the angle in center-of-mass frame. The lines are calculated from a local potential fit which is adjusted to the scattering data (full black line) and from different global α-nucleus potentials [16,18,19] (MCF: blue dotted; AVR: red dash-dotted; ATOMKI-V1: green dashed). The experimental data are taken from [12,13]. The given energies are $E_{\text{c.m.}}$ in the center-of-mass system.
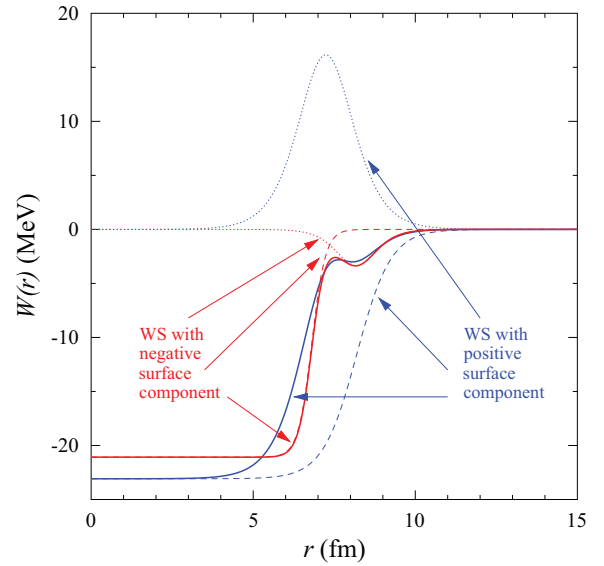

FIG. 2. (Color online) Ambiguity of the imaginary potential, illustrated for the analysis of the angular distribution at $E = 31.11$ MeV. The imaginary potentials of two different fits (shown in blue and red full lines) are very similar. However, the decomposition into the volume (thin dashed) and surface (thin dotted) components shows that in one case there is a weak negative surface term (red) whereas in the other case a strong positive surface term (blue) is found.

average. However, there is no systematic energy dependence of R_S and a_S which may lead to uncertainties in the extrapolation of the potential down to very low energies (see also Sec. III B). The depth parameter W_S and the imaginary volume integral J_I increase with energy for the lowest three energies.

At higher energies above 30 MeV, the best χ^2/F is obtained from a combination of a volume and a surface Woods-Saxon potential. At all energies above 30 MeV the volume term is dominating. An interesting ambiguity in the parametrization of the imaginary potential is found for the combination of volume and surface Woods-Saxon potentials. Very similar potentials can be obtained using a positive or a negative surface term. This is illustrated in Fig. 2 for the analysis at $E = 31.11$ MeV. In the first fit (parameters given in Table II) the usual behavior is found: the weak negative surface component modifies the dominating volume component in the surface region around

8 fm. However, in the second fit (parameters: $\lambda = 1.269$, $w = 1.004$, $W_V = -23.1$ MeV, $R_V = 1.579$ fm, $a_V = 0.525$ fm, $W_S = -64.6$ MeV, $R_S = 1.394$ fm, $a_S = 0.571$ fm, $\sigma_{\text{reac}} = 1464$ mb) a relatively strong and positive surface contribution is found. But the total imaginary part is very similar in both fits, in particular in the most relevant surface region, and thus also the resulting χ^2/F and derived σ_{reac} are practically identical. Such an ambiguity is found at all energies above 30 MeV. In principle, the fit with the lowest χ^2/F should be used for the extraction of σ_{reac} from the experimental angular distribution. However, because the found χ^2/F minima are very similar and do not differ by more than 10%, and because the derived σ_{reac} are stable within 1%, the fits with the usual negative surface component are listed in Table II. This choice should avoid further complications, e.g., when using these parameters for the construction of a global potential. For completeness it is pointed out that fits with a pure volume Woods-Saxon imaginary potential have a worse χ^2/F, and the derived σ_{reac} vary within several percent.

It is obvious that the energy dependence of J_I and the shape of the imaginary part of the potential are dominating sources for uncertainties of cross section predictions at very low energies. As usual, the imaginary potential $W(r)$ is dominated by the surface contribution at low energies, and its volume integral J_I increases with energy. At higher energies above 30 MeV the volume contribution becomes dominant. The data at 23.30 MeV could also be fitted using a combination of volume ($W_V = -13.8$ MeV, $R_V = 1.30$ fm, $a_V = 0.81$ fm) and surface ($W_S = 13.6$ MeV, $R_S = 1.58$ fm, $a_S = 0.34$ fm) potential, i.e., with a further decreasing volume contribution. Although the number of adjustable parameters is larger, this

fit did not lead to an improved description of the angular distribution (no significant improvement of χ^2/F). Therefore, from this energy down to lowest energies only a surface imaginary potential was used. This choice is confirmed by the fact that an excellent reproduction of all angular distributions below 25 MeV with $\chi^2/F \lesssim 1$ has been achieved using a pure surface Woods-Saxon potential in the imaginary part. Because the volume integrals J_I increase with energy at these low energies, a similar behavior is found for the strength of the surface imaginary potential W_S.

The influence of uncertainties in the real part and the imaginary part on the calculation of the total reaction cross section σ_{reac} will be investigated in further detail later (see Sec. III).

The elastic scattering angular distributions are also compared to predictions from several global α-nucleus optical potentials. In Fig. 1 we show the very simple four-parameter potential by McFadden and Satchler (MCF) [19], the many-parameter potential by Avrigeanu (AVR) [16], and the recent first version of the ATOMKI potential (ATOMKI-V1) [18]. For illustration, I also show the real and imaginary nuclear potentials for the lowest energy of 14.28 MeV and an intermediate energy (31.11 MeV) in Fig. 3.

III. DETERMINATION OF THE TOTAL REACTION CROSS SECTION σ_{reac} AND THE REDUCED CROSS SECTION σ_{red}

A. Extraction of σ_{reac} and σ_{red} from the experimental angular distributions

The total reaction cross sections σ_{reac} are derived from these local fits using Eq. (1). For an estimation of the uncertainty of σ_{reac} an additional model-independent phase shift analysis (PSA) has been performed using the technique of [26]. The total reaction cross sections σ_{reac} from the PSA are close to the results of the local potential fit. A typical uncertainty for σ_{reac} of about 3% is estimated (see also [27]) except at very low energies significantly below the Coulomb barrier.

It is interesting to note that there is only a relatively weak dependence of the derived total reaction cross section σ_{reac} on the absolute normalization of the elastic scattering angular distribution. At relatively low energies the absolute normalization is well defined from Rutherford scattering at forward angles. This is the case for all energies under study in this work. But even at energies far above the Coulomb barrier it turns out that the potentials are relatively well defined by the diffraction pattern in the angular distribution. Consequently the extracted σ_{reac} vary typically by less than 10% even for strong variations of the absolute normalization of up to 30%.

In general, the extraction of the total reaction cross section σ_{reac} from elastic scattering angular distributions requires theoretical considerations and is thus somewhat model-dependent. But because of the small sensitivity of σ_{reac} to the chosen model, the total reaction cross section σ_{reac} can be considered as a quasiexperimental quantity. This holds in particular for the present case where the elastic scattering angular distributions cover a wide angular range and the scattering energies are not extremely low. These quasiexperimental total reaction
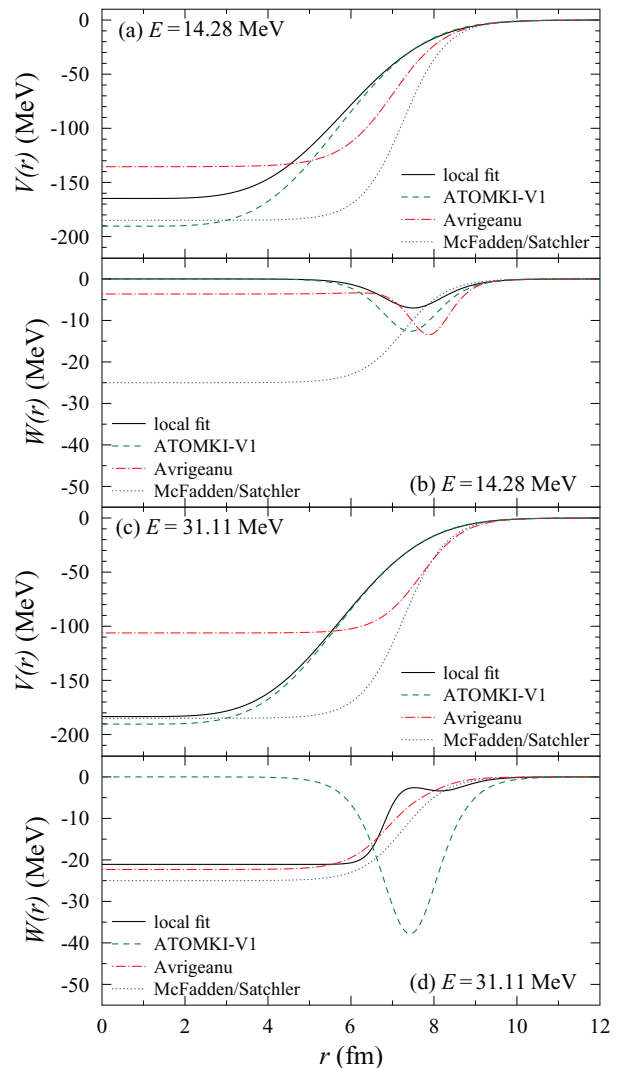

FIG. 3. (Color online) Real part (a,c) and imaginary part (b,d) of the underlying potentials for the angular distributions at 14.28 MeV (a,b) and 31.11 MeV (c,d) from the local fit (black full line) and the global potentials [16,18,19] (MCF: blue dotted; AVR: red dash-dotted; ATOMKI-V1: green dashed; colors and linestyles identical to Fig. 1). A decomposition of the best-fit potential at 31.11 MeV into its volume and surface components is also given in Fig. 2.

cross sections are compared to predictions of global α-nucleus potentials in Table III. The very simple MCF potential [19], the many-parameter AVR potential [16], and the few-parameter ATOMKI-V1 potential [18] provide almost identical σ_{reac} in good agreement with the experimental results although the reproduction of the experimental angular distributions is not perfect in some cases (see Fig. 1). Obviously, the global potentials (which are not fitted to the data) cannot reproduce the experimental angular distributions with the same quality as the local fit. In particular, the ATOMKI-V1 potential has been adjusted to low-energy scattering data only. This leads to a relatively poor description of the experimental angular distributions at higher energies because of the missing volume term in the imaginary part. However, even deviations in the angular distribution of up to one order of magnitude at very

TABLE III. Experimental total reaction cross sections σ_{reac} (in mb) derived from $^{140}\text{Ce}(\alpha,\alpha)^{140}\text{Ce}$ elastic scattering angular distributions (from Table II), compared to predictions from the global α-nucleus potentials MCF [19], AVR [16], and ATOMKI-V1 [18]. For a discussion of the $^{143}\text{Nd}(n,\alpha)^{140}\text{Ce}$ data see Sec. IV.

$E_{\text{c.m.}}$ (MeV)	exp.	MCF	AVR	ATOMKI-V1
10.0[a]	$(1.9 \pm 0.4\,\mu\text{b})$[b]	$9.3\,\mu\text{b}$	$0.7\,\mu\text{b}$	$4.5\,\mu\text{b}$
14.28	28 ± 4	26	23	24
18.47	399 ± 30	464	477	460
23.30	999 ± 30	987	1025	989
31.11	1453 ± 44	1472	1508	1494
36.65	1824 ± 55	1676	1712	1712
43.75[c]	1940 ± 97	1852	1883	1903

[a]Corresponds to the low-energy $^{143}\text{Nd}(n,\alpha)^{140}\text{Ce}$ data.
[b]Derived from the low-energy $^{143}\text{Nd}(n,\alpha)^{140}\text{Ce}$ data.
[c]Natural cerium (^{140}Ce: 88.48%).

backward angles do not prevent the prediction of σ_{reac} with minor uncertainties.

The similarity of the total reaction cross sections σ_{reac} from the different global potentials can be understood from a semiclassical interpretation of the reflexion coefficients η_L in the partial wave analysis. The following discussion will focus on the shown energies of 31.11 MeV above the Coulomb barrier and 14.28 MeV below the Coulomb barrier (see Fig. 3 for the potentials and Fig. 4 for the reflexion coefficients η_L and the contributions σ_L of the Lth partial wave to σ_{reac}). The discussion extends a similar study in [10].

Small angular momenta L correspond to small impact parameters or central collisions. At energies above the Coulomb barrier the incoming α particles are able to reach the interior, and the corresponding partial waves are almost fully absorbed: $\eta_L \approx 0$ for $L \lesssim 10$ and thus $\sigma_L \approx \sigma_{L,\text{max}} = (2L+1)\pi/k^2$. The linear increase of σ_L is nicely seen in Fig. 4 (indicated by the dashed brown line). Consequently, only very few α particles are scattered into the backward angular region where the cross section is found to be much smaller than the Rutherford cross section.

Large angular momenta L correspond to large impact parameters or peripheral collisions and scattering to forward angles. These partial waves do not reach the nuclear interior and are thus practically not absorbed: $\eta_L \approx 1$ and $\sigma_L \approx 0$ is found for $L \gtrsim 20$.

Potentials have to fulfill two simple criteria to provide σ_{reac} above the Coulomb barrier with sufficient accuracy. First, the potential must have the correct short range; then $\eta_L \approx 1$ for $L \gtrsim 20$ is automatically obtained. Second, the imaginary part must be sufficiently strong to guarantee $\eta_L \approx 0$ for $L \lesssim 10$. These two simple criteria are necessary but not yet sufficient for an excellent α-nucleus potential which should simultaneously describe elastic angular distributions with reasonable χ^2/F. Both simple criteria are fulfilled by all global potentials in this study. The origin for differences in σ_{reac} from different realistic potentials can only stem from a few η_L or σ_L for intermediate angular momenta $10 \lesssim L \lesssim 20$. But even in this intermediate L range the σ_L have to decrease from $\sigma_{L,\text{max}}$ down to $\sigma_L \approx 0$. Thus, it is not at all surprising
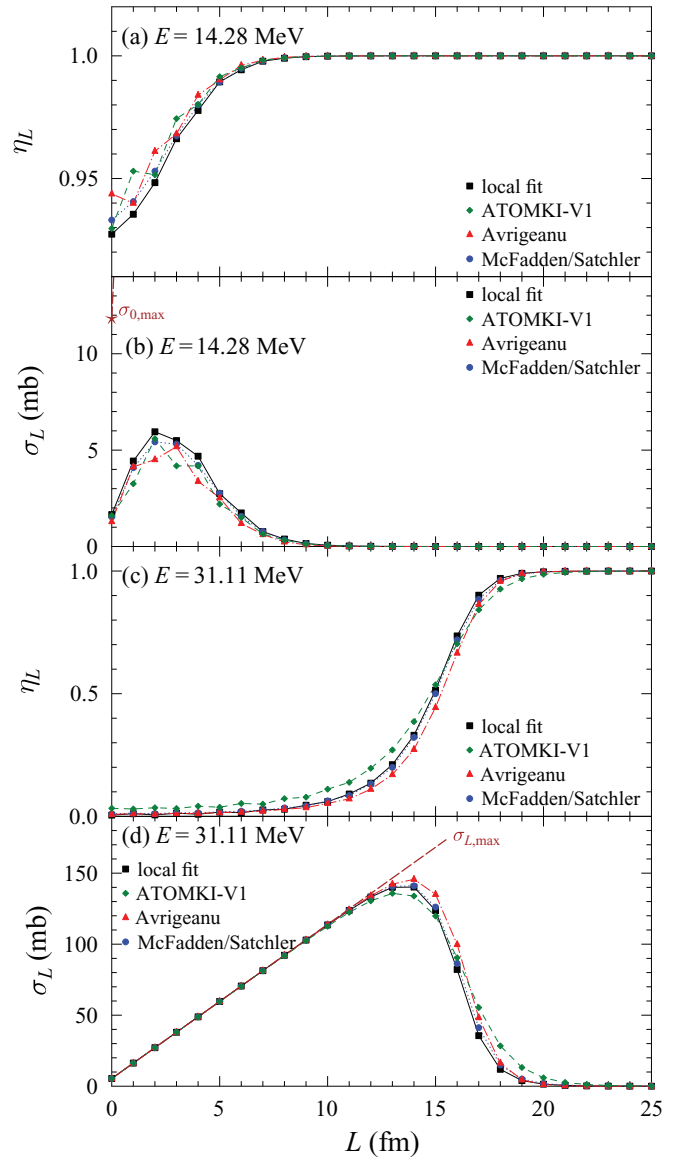

FIG. 4. (Color online) Reflexion coefficients η_L (a,c) and contributions σ_L of the Lth partial wave to the total reaction cross section σ_{reac} (b,d) for the angular distributions at 14.28 MeV (a,b) and 31.11 MeV (c,d). The data are obtained from the local fit (full black squares) and from the global potentials under study [16,18,19] (MCF: blue circles; AVR: red triangles; ATOMKI-V1: green diamonds; colors are identical to Fig. 1). The data points are connected by thin colored lines to guide the eye. The maximum values $\sigma_{L,\text{max}}$ are indicated as thick dashed brown line [31.11 MeV, (d)] and as data point for $\sigma_{0,\text{max}}$ [14.28 MeV, (b)]. Further discussion see text.

that different global potentials provide very similar σ_{reac} at energies above the Coulomb barrier. As a test I have increased the imaginary part of the local potential at 31.11 MeV by a factor of 2 and a factor of 10. As expected, this leads to only very moderate enhancements of the total reaction cross section σ_{reac} by about 1% and 8% although the corresponding elastic angular distributions change by more than one order of magnitude in the backward angular region.

The situation is much different at lower energies below the Coulomb barrier. Again, partial waves with large angular momenta L are not much affected by any short-range potential, and $\eta_L \approx 1$ is found. However, even α particles with small impact parameters will mostly not be able to tunnel through the Coulomb barrier. Thus, the elastic cross section at backward angles rises and approaches the Rutherford cross section, and the η_L remain close to unity even for small L. The total cross section σ_{reac} is now composed of the contributions from a few partial waves with low $L \lesssim 8$ in the chosen example of 14.28 MeV. It is surprising that even under these conditions the various potentials under study provide very similar σ_{reac} (see Table III), and indeed significant variations have been found in the analysis of the recent $^{141}\text{Pr}(\alpha,n)^{144}\text{Pm}$ reaction data at slightly lower energies [9,10].

B. Sensitivity of σ_{reac} to details of the optical potential

Let me now artificially decompose the absorption into an interior contribution ($r \lesssim R_\alpha + R_{^{140}\text{Ce}}$) and an exterior contribution ($r \gg R_\alpha + R_{^{140}\text{Ce}}$). It is the aim of this analysis to find out the radial range of the potential which mainly defines σ_{reac}. A semiclassical decomposition as, e.g., presented in [28] may be misleading here because the semiclassical approximation deviates from a fully quantum-mechanical calculation by several percent [28] which is not acceptable at very low energies. For completeness it has also to be pointed out that "exterior" in the above sense means radii above $\approx (10–12)$ fm where the nuclear real and imaginary potentials have practically dropped to values close to zero (see Fig. 3). Consequently, "interior" corresponds to the radial range where the nuclear potentials deviate from zero, and "interior absorption" is dominated by the surface absorption by the surface imaginary potential.

The interior contribution requires that the incoming α particle tunnels through the Coulomb barrier and reaches an area where it is absorbed by the imaginary part of the potential. It is thus mainly sensitive to the shape of the Coulomb barrier which in turn is defined by the exterior of the real part of the nuclear potential whereas details of the imaginary part are not so important. This is similar to the full absorption for small L at higher energies, but only very few α particles are able to tunnel through the Coulomb barrier at very low energies. An exterior contribution is obtained from the tail of the imaginary potential for large radii; it does practically not depend on the real part. This tail is weak but affects all incoming α particles. The relative importance of the interior and exterior contributions can be estimated by a variation of the strengths of the real and imaginary nuclear potentials or by introducing a cutoff radius R_{cut} for the imaginary potential [$W(r) = 0$ for $r > R_{\text{cut}}$].

It is found that at energies around 12 MeV an enhancement of the real part by a factor of two increases σ_{reac} by a factor of about 3 whereas an enhancement of the same factor of two for the imaginary part increases σ_{reac} only by about 40%; i.e., the interior absorption is dominating at these energies. This is confirmed by the fact that a cutoff for the imaginary potential at $R_{\text{cut}} = 12$ fm reduces σ_{reac} by less than 10%.

At much lower energies the relative contribution of the exterior absorption increases, and at about 6 MeV it is found that a factor of two enhancement of the real part and the imaginary part both lead to the same factor of two enhancement for σ_{reac}. A cutoff radius of $R_{\text{cut}} = 12$ fm for the imaginary part now reduces σ_{reac} by about a factor of 6, and even a huge $R_{\text{cut}} = 15$ fm still leads to a reduction of σ_{reac} by almost a factor of two.

In other words this means that the prediction of σ_{reac} at very low energies requires detailed knowledge of the nuclear potential at very large distances. The real part at large distances is essential for the internal contribution at energies of about 10–15 MeV, and the imaginary part at large distances is important for the external contribution which dominates at very low energies far below 10 MeV. However, the sensitivity of elastic scattering data to the potential at large radii is limited. It is obvious that the reproduction of σ_{reac} is a necessary requirement for any global potential; but this requirement is almost automatically fulfilled at energies above the Coulomb barrier. Further investigation is needed on the question whether such a global potential is able to predict reaction cross sections of α-induced reactions below the Coulomb barrier. It remains an open question which deviation (e.g., in χ^2/F) remains allowed in the description of elastic scattering data to ensure a reasonable prediction of low-energy α-induced reaction cross sections. In this context an interesting example is the potential of Fröhlich and Rauscher [31]; it has been optimized for the calculation of reaction cross sections and works very well for this purpose, but it shows larger deviations than other global potentials in the analysis of elastic scattering angular distributions.

Table III shows that the relative uncertainty of σ_{reac} increases strongly with decreasing energy. This is not surprising because the elastic scattering angular distribution approaches the Rutherford cross section at low energies. This holds in particular for the lowest energy where the ratio to the Rutherford cross section is above 0.8 even at the most backward angles; thus, very precise data are required here. Unfortunately, these data of Watson *et al.* [12] are not available numerically and have been extracted from Fig. 2 of [12] in the EXFOR [14] database. Using these EXFOR data leads to poor fits with parameters outside the expected range and $\sigma_{\text{reac}} \approx 65$ mb. I have carefully repeated the digitization of the data in Fig. 2 of [12], and I have obtained significantly larger elastic cross sections at backward angles. Now the fit provides parameters in the expected range, and I find a smaller total reaction cross section of $\sigma_{\text{reac}} = 28.1$ mb. It is interesting to note that the original analysis in [12] using a Woods-Saxon potential gives an almost identical total reaction cross section of $\sigma_{\text{reac}} = 27.8$ mb. This confirms the newly digitized data. These revised data will be sent to EXFOR.

For comparison of various targets at different energies, often reduced total reaction cross sections $\sigma_{\text{red}} = \sigma_{\text{reac}}/(A_P^{1/3} + A_T^{1/3})^2$ are plotted versus the reduced energy $E_{\text{red}} = (A_P^{1/3} + A_T^{1/3})E_{\text{c.m.}}/(Z_P Z_T)$, see, e.g., [27,29]. The data for many α-nucleus systems are shown in Fig. 5. It is obvious that the new data for ^{140}Ce fit nicely into the global systematics. Furthermore, it can be seen that various global potentials
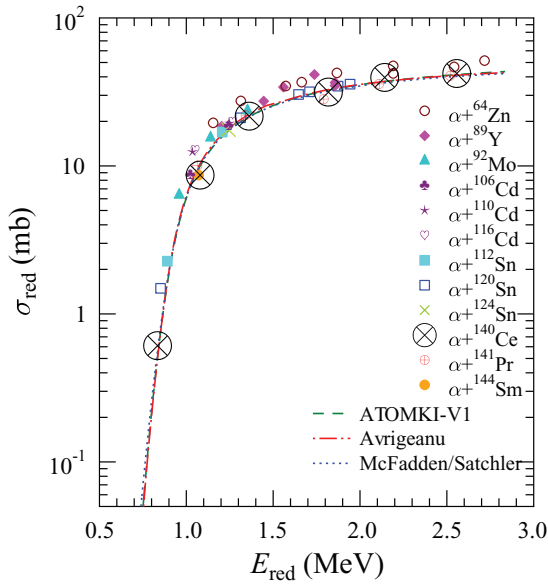
FIG. 5. (Color online) Reduced reaction cross sections σ_{red} versus reduced energy E_{red} for various α-nucleus systems [10,18,27], compared to predictions from global α-nucleus potentials [16,18,19]. The experimental data are taken from [12,13] for ^{140}Ce and from [15] for natural cerium. The predictions are almost identical in the shown energy range. The indirect data point at 10 MeV from the ^{143}Nd$(n,\alpha)^{140}$Ce reaction is located far below the shown region ($E_{\text{red}} = 0.584$ MeV, $\sigma_{\text{red}} = 4.0 \times 10^{-5}$ mb).

[16,18,19] provide almost identical σ_{red} in the energy range above $E_{\text{red}} \gtrsim 0.8$ MeV ($E_{\text{c.m.}} \gtrsim 13.7$ MeV) whereas significant deviations between the different potentials are only found at very low energies. It should be kept in mind that at these very low energies ($E_{\text{red}} \ll 0.8$ MeV) the total reaction cross section is dominated by inelastic scattering, mainly by Coulomb excitation, but not by compound formation.

C. Lower energy limit for the determination of σ_{reac}

The extraction of σ_{reac} from elastic scattering angular distributions is possible with reasonable uncertainties as long as the deviation from the Rutherford cross section exceeds the experimental uncertainties significantly. The Watson data at 15 MeV fulfill this requirement with $\sigma/\sigma_R \approx 0.8$ (i.e., a deviation from Rutherford of about 20%) at backward angles and claimed experimental uncertainties of less than 5%. However, at slightly lower energies the extraction of σ_{reac} becomes impossible even with typical uncertainties of up-to-date high-precision scattering data [18,30] which are still of the order of a few percent (systematic plus statistical uncertainties).

A test calculation has been made at $E_{\text{lab}} = 14.0$ MeV ($E_{\text{c.m.}} = 13.61$ MeV) in the following way. First, the angular distribution at this energy is calculated from the ATOMKI-V1 potential from $20°$ to $175°$ in steps of $5°$. Here I find $\sigma/\sigma_R \approx 0.94$ at the most backward angles. Next, several virtual experimental data sets are created from this angular distribution by randomly varying each data point within its uncertainty (Gaussian distribution with an assumed 3%
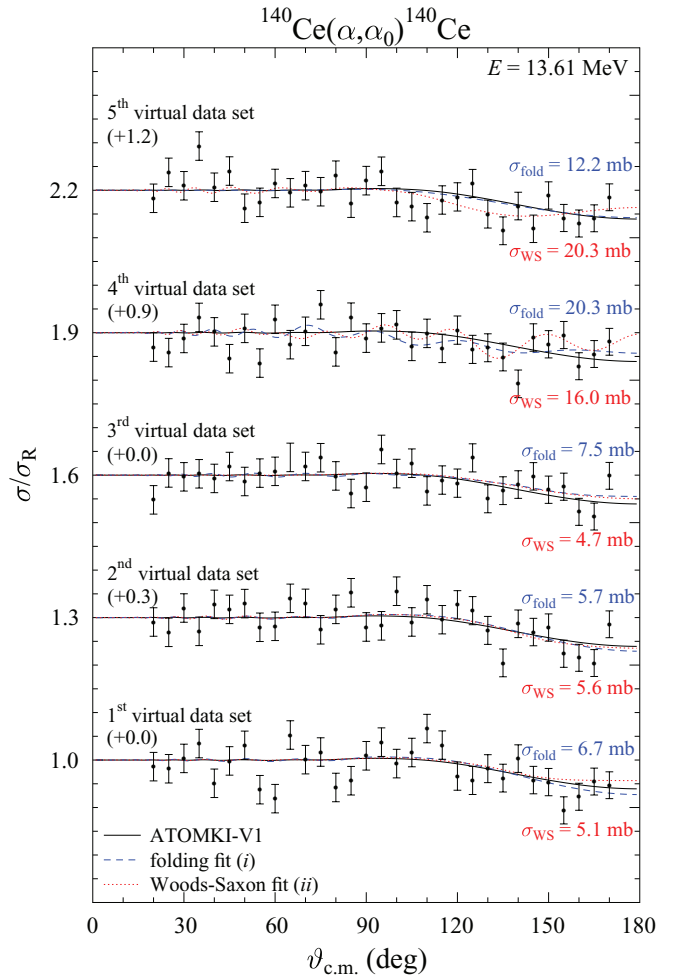

FIG. 6. (Color online) Rutherford normalized elastic scattering cross sections of ^{140}Ce$(\alpha,\alpha)^{140}$Ce versus $\vartheta_{\text{c.m.}}$ at $E_{\text{c.m.}} = 13.61$ MeV. Various virtual data sets are created from the ATOMKI-V1 potential (full black line) by a random variation of the data points within an assumed 3% uncertainty, and they are analyzed to estimate the uncertainty of the derived total reaction cross section σ_{reac} using either a folding potential in the real part (case i, blue dashed) or volume Woods-Saxon potentials (case ii, red dotted). Further discussion see text.

1-σ uncertainty, corresponding to the most precise available scattering data [18,30]). Finally, the various virtual data sets are analyzed in the usual way by fitting the parameters of the optical potential. Here I use two parametrizations: (i) a folding potential in the real part and a surface Woods-Saxon potential in the imaginary part (i.e., the same parametrization as the underlying ATOMKI-V1 potential), and (ii) a volume Woods-Saxon potential in the real and in the imaginary part. The results are shown in Fig. 6. As expected, it is found that the fits become relatively unstable, and restrictions on the number of fitted parameters have to be used. The obtained total reaction cross sections from the fits to the virtual data sets vary between about 5 and 20 mb (i.e., vary by a factor of 4) whereas the starting value from the ATOMKI-V1 potential was 8.8 mb. Thus, the uncertainty for the derived σ_{reac} is at least a factor of 2 at the low energy of $E_{\text{c.m.}} = 13.61$ MeV which

is dramatically larger than the about 15% uncertainty obtained at the slightly higher energy of 14.28 MeV. However, the largest deviations for σ_{reac} are correlated with extreme fitting parameters and unusually oscillating angular distributions (e.g., in the case of the fourth virtual data set). Constraining the resulting parameters to a reasonable range may allow to determine σ_{reac} even in the case of the fourth virtual data set; but such constraints put into question whether this is still a model-independent determination of σ_{reac}.

A simple constraint might be to fix the geometry of the potentials from data at higher energies, e.g., by taking the average values of w in the real part and R_S and a_S in the imaginary part from Table II. Then only two parameters (λ and W_S) remain to be adjusted to the data sets. However, even in this very restricted parameter space total reaction cross sections σ_{reac} between about 5 and 20 mb have been found, and it remains necessary to keep λ and W_S close to their expected values to obtain values of σ_{reac} close to the initial $\sigma_{\mathrm{reac}} = 8.8$ mb. So the lower limit for the determination of σ_{reac} seems to be reached around $E \approx 13.5$ MeV even if high-quality scattering data are available over the full angular range.

IV. A SHORT NOTE ON THE ^{143}ND$(n,\alpha)^{140}$CE REACTION

Recently, experimental data for the ^{143}Nd$(n,\alpha)^{140}$Ce reaction have been measured at energies below 1 MeV [32] and between 4 and 6 MeV [33], and earlier data below 10 MeV are available from [34] and [35]. The calculation of the ^{143}Nd$(n,\alpha)^{140}$Ce reaction cross section in the statistical model requires the knowledge of the ^{140}Ce-α potential. Because of the huge positive Q value of 9.72 MeV, this potential has to be determined at energies around 15 MeV for the higher-energy data in [33]. This is exactly the energy range of the Watson *et al.* scattering data [12] where the various potentials under study were able to reproduce σ_{reac} within about 15–20% (see Table III). Thus, the uncertainty from the α-nucleus potential in the calculation of the ^{143}Nd$(n,\alpha)^{140}$Ce reaction remains very limited. I have calculated the cross sections using the default parameters of TALYS V1.4 [36] and the MCF potential in the α channel. The result is shown in Fig. 7. The agreement with the experimental data above 1 MeV [33,34] is reasonable although the energy dependence of the data points is not perfectly reproduced. At energies below 1 MeV the experimental data of [32,35] are overestimated which is a typical behavior for the MCF potential at energies significantly below the Coulomb barrier, see, e.g., for ^{144}Sm$(\alpha,\gamma)^{148}$Gd [1], ^{141}Pr$(\alpha,n)^{144}$Pm [9,10], ^{112}Sn$(\alpha,\gamma)^{116}$Te [3], and ^{106}Cd$(\alpha,\gamma)^{110}$Sn [2].

The calculations have been repeated using the code SMARAGD [37] with its default parameters (here the MCF potential is used in the α channel by default), see Fig. 7, brown line. As pointed out in [38], the ^{143}Nd$(n,\alpha)^{140}$Ce reaction cross section is mainly sensitive to the optical potential in the α channel whereas the other ingredients of the statistical model codes have only minor influence on the (n,α) cross section (for details see the sensitivity figures shown in Ref. [39]). As expected, the two codes provide very similar results for energies below 1 MeV. However, above 1 MeV surprisingly significant differences up to a factor of two appear.
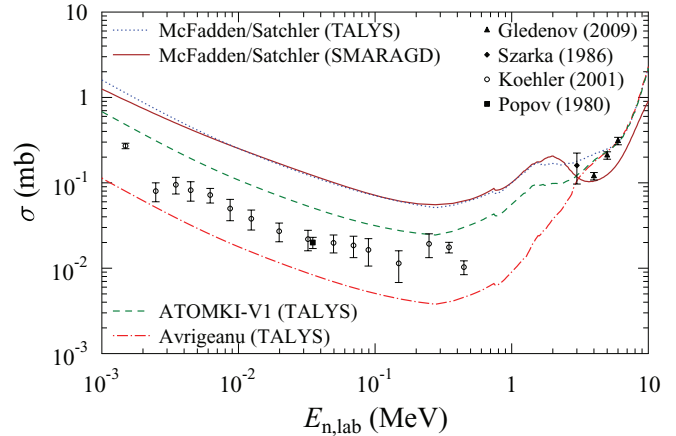

FIG. 7. (Color online) Cross section of the ^{143}Nd$(n,\alpha)^{140}$Ce reaction. The experimental data are taken from [32–35]. Calculations have been performed using the MCF potential in the statistical model codes TALYS [36] (blue dotted) and SMARAGD [37] (full brown). The results for the ATOMKI-V1 (green dashed) and AVR (red dash-dotted) potentials are derived from the TALYS results. Further discussion see text.

Interestingly, the SMARAGD calculation shows a similar energy dependence as the experimental data points [33,34] but it underestimates the absolute scale significantly. It is beyond the scope of the present paper to provide a detailed comparison of the TALYS and SMARAGD codes. The disagreement between both codes may be related to the treatment of excited states in the exit channel (i.e., in the ^{140}Ce nucleus); this sensitivity is not explicitly studied in [39]. But different choices of this treatment in TALYS lead only to minor variations of about 20% for the (n,α) cross section and cannot explain the factor of two discrepancy between TALYS and SMARAGD. Therefore, great care is required in the determination of the α-nucleus potential from low-energy reaction data because the influence of other ingredients on the calculated cross sections has to be investigated in detail.

Nevertheless, the influence of different potentials on the ^{143}Nd$(n,\alpha)^{140}$Ce reaction cross section can be studied at low energies below 1 MeV where TALYS and SMARAGD show the expected agreement for the MCF potential. It is found that the MCF potential overestimates the experimental data by a factor of 5. As this energy range below 1 MeV corresponds to energies in the α channel of about 10 MeV, it is possible to estimate σ_{reac} at this energy because σ_{reac} is only sensitive to the chosen α-nucleus potential: $\sigma_{\mathrm{reac}} \approx 1.9 \pm 0.4\,\mu$b. For comparison, the predictions from the different potentials under study at 10 MeV are also listed in Table III.

It is technically difficult to use the ATOMKI-V1 folding potential in the TALYS or SMARAGD codes. However, because the (n,α) cross section is practically sensitive only to the α-potential [38,39], it is possible to calculate the ^{143}Nd$(n,\alpha)^{140}$Ce cross section for the ATOMKI-V1 potential by scaling the MCF result with the ratio of the total cross sections σ_{reac} of the ATOMKI-V1 potential and the MCF potential at the corresponding energy in the α channel. The same method has been applied for the AVR potential. In both cases the underlying MCF result has been taken from the TALYS

calculation. The results are compared to the experimental data of [32–35] in Fig. 7. At energies below 1 MeV the ATOMKI-V1 potential slightly overestimates the experimental data of [32,35] whereas the AVR potential slightly underestimates the data. But both potentials are much closer to the experimental data than the MCF potential which predicts the (n,α) cross section about a factor of two higher than the ATOMKI-V1 potential and more than one order of magnitude higher then the AVR potential.

For the data in the MeV region [33,34] (corresponding to the 15 MeV region in the α channel) all potentials under study provide almost identical total reaction cross sections σ_{reac}, and thus the calculated (n,α) cross sections are very similar. It is not possible to extract information on the potential in this energy range. This holds in particular as long as significant differences appear between the two widely used codes TALYS and SMARAGD. Finally, it is interesting to note that almost the same behavior of the MCF (overestimation), AVR (slight underestimation), and ATOMKI-V1 (slight overestimation; not shown in [10]) potentials is found in the analysis [10] of the recent ^{141}Pr$(\alpha,n)^{144}$Pm data [9].

V. SUMMARY AND CONCLUSIONS

Angular distributions of ^{140}Ce$(\alpha,\alpha)^{140}$Ce elastic scattering were analyzed in the framework of the optical model. Excellent fits were obtained using locally adjusted parameters of the real folding and imaginary Woods-Saxon potentials. Total reaction cross sections σ_{reac} were derived from the local fits using Eq. (1). The new data are in excellent agreement with the systematics of reduced cross sections σ_{red} [18,27].

It was shown that various global α-nucleus potentials predict the total reaction cross sections σ_{reac} very well although the predicted angular distributions do not agree perfectly with the experimental angular distributions and may even deviate by up to an order of magnitude at very backward angles. Thus, at least at energies above about 15 MeV, the α-nucleus potential is not the major source of uncertainties in the calculation of α-induced reaction cross sections in the statistical model. This can be understood by a semiclassical interpretation of the partial wave analysis.

It is highlighted that data with very small uncertainties are required for the extraction of σ_{reac} at low energies where the elastic scattering angular distribution approaches the Rutherford cross section. As the analysis of the Watson *et al.* data [12] shows, special diligence is required for data which are taken from published figures by digitization. An extraction of σ_{reac} from elastic scattering angular distributions becomes impossible with a reasonable uncertainty as soon as the deviation from the Rutherford cross section at backward angles becomes smaller than the experimental uncertainty.

Finally, further information on the α-nucleus potentials at very low energies can be extracted only from the analysis of reaction data. Although great care is required for such an analysis because of the influence of other ingredients of the statistical model calculations, it can be concluded from the low-energy ^{143}Nd$(n,\alpha)^{140}$Ce data below $E_n = 1$ MeV that the recent ATOMKI-V1 and AVR potentials provide a significant improvement around $E \approx 10$ MeV in the α channel, i.e., far below the Coulomb barrier, whereas the MCF potential overestimates the ^{143}Nd$(n,\alpha)^{140}$Ce data by a factor of 5.

[1] E. Somorjai, Zs. Fülöp, A. Z. Kiss, C. E. Rolfs, H.-P. Trautvetter, U. Greife, M. Junker, S. Goriely, M. Arnould, M. Rayet, T. Rauscher, and H. Oberhummer, Astron. Astrophys. **333**, 1112 (1998).

[2] Gy. Gyürky, G. G. Kiss, Z. Elekes, Zs. Fülöp, E. Somorjai, A. Palumbo, J. Görres, H. Y. Lee, W. Rapp, M. Wiescher, N. Özkan, R. T. Güray, G. Efe, and T. Rauscher, Phys. Rev. C **74**, 025805 (2006).

[3] N. Özkan, G. Efe, R. T. Güray, A. Palumbo, J. Görres, H. Y. Lee, L. O. Lamm, W. Rapp, E. Stech, M. Wiescher, Gy. Gyürky, Zs. Fülöp, and E. Somorjai, Phys. Rev. C **75**, 025801 (2007).

[4] I. Cata-Danil, D. Filipescu, M. Ivascu, D. Bucurescu, N. V. Zamfir, T. Glodariu, L. Stroe, G. Cata-Danil, D. G. Ghita, C. Mihai, G. Suliman, and T. Sava, Phys. Rev. C **78**, 035803 (2008).

[5] C. Yalcin, R. T. Güray, N. Özkan, S. Kutlu, Gy. Gyürky, J. Farkas, G. G. Kiss, Zs. Fülöp, A. Simon, E. Somorjai, and T. Rauscher, Phys. Rev. C **79**, 065801 (2009).

[6] Gy. Gyürky, Z. Elekes, J. Farkas, Zs. Fülöp, Z. Halász, G. G. Kiss, E. Somorjai, T. Szücs, R. T. Güray, N. Özkan, C. Yalcin, and T. Rauscher, J. Phys. G **37**, 115201 (2010).

[7] G. G. Kiss, T. Rauscher, T. Szücs, Zs. Kertész, Zs. Fülöp, Gy. Gyürky, C. Fröhlich, J. Farkas, Z. Elekes, and E. Somorjai, Phys. Lett. B **695**, 419 (2011).

[8] G. G. Kiss, T. Szücs, Zs. Török, Z. Korkulu, Gy. Gyürky, Z. Halász, Zs. Fülöp, E. Somorjai, T. Rauscher, Phys. Rev. C **86**, 035801 (2012).

[9] A. Sauerwein, H. W. Becker, H. Dombrowski, M. Elvers, J. Endres, U. Giesen, J. Hasper, A. Hennig, L. Netterdon, T. Rauscher, D. Rogalla, K. O. Zell, and A. Zilges, Phys. Rev. C **84**, 045808 (2011).

[10] P. Mohr, Phys. Rev. C **84**, 055803 (2011).

[11] Gy. Gyürky, P. Mohr, Zs. Fülöp, Z. Halász, G. G. Kiss, T. Szücs, and E. Somorjai, Phys. Rev. C **86**, 041601(R) (2012).

[12] B. D. Watson, D. Robson, D. D. Tolbert, and R. H. Davis, Phys. Rev. C **4**, 2240 (1971).

[13] P. Guazzoni and L. Zetta, private communication to G. Staudt, 1994 (unpublished).

[14] EXFOR database, http://www-nds.iaea.org/exfor/exfor.htm version September 21, 2012.

[15] F. T. Baker and R. Tickle, Phys. Rev. C **5**, 182 (1972).

[16] M. Avrigeanu and V. Avrigeanu, Phys. Rev. C **82**, 014606 (2010).

[17] M. Avrigeanu, A. C. Obreja, F. L. Roman, V. Avrigeanu, and W. von Oertzen, At. Data Nucl. Data Tables **95**, 501 (2009).

[18] P. Mohr, G. G. Kiss, Zs. Fülöp, D. Galaviz, Gy. Gyürky, and E. Somorjai, At. Data Nucl. Data tables accepted for publication; arXiv:1212.2891.

[19] L. McFadden and G. R. Satchler, Nucl. Phys. **84**, 177 (1966).

[20] U. Atzrott, P. Mohr, H. Abele, C. Hillenmayer, and G. Staudt, Phys. Rev. C **53**, 1336 (1996).

[21] H. de Vries, C. W. de Jager, and C. de Vries, At. Data and Nucl. Data Tables **36**, 495 (1987).

[22] B. L. Miller, L. S. Cardman, C. N. Papanicolas, T. E. Milliman, J. P. Connelly, J. H. Heisenberg, F. W. Hersman, J. E. Wise, B. Frois, D. Goutte, and V. Meot, Phys. Rev. C **37**, 895 (1988).

[23] W. Kim, B. L. Miller, J. R. Calarco, L. S. Cardman, J. P. Connelly, S. A. Fayans, B. Frois, D. Goutte, J. H. Heisenberg, F. W. Hersman, V. Meot, T. E. Milliman, P. Mueller, C. N. Papanicolas, A. P. Platonov, V. Yu. Ponomarev, and J. E. Wise, Phys. Rev. C **45**, 2290 (1992).

[24] B. L. Miller, Ph.D. thesis, University of Illinois at Urbana-Champaign, 1994 (unpublished); available at http://hdl.handle.net/2142/18865.

[25] P. Mohr, Phys. Rev. C **61**, 045802 (2000).

[26] V. Chisté, R. Lichtenthäler, A. C. C. Villari, and L. C. Gomes, Phys. Rev. C **54**, 784 (1996).

[27] P. Mohr, D. Galaviz, Zs. Fülöp, Gy. Gyürky, G. G. Kiss, and E. Somorjai, Phys. Rev. C **82**, 047601 (2010).

[28] D. M. Brink and N. Takigawa, Nucl. Phys. A **279**, 159 (1977).

[29] P. N. de Faria *et al.*, Phys. Rev. C **81**, 044605 (2010).

[30] A. Palumbo *et al.*, Phys. Rev. C **85**, 035808 (2012).

[31] T. Rauscher, Nucl. Phys. A **719**, 73c (2003).

[32] P. E. Koehler, Yu. M. Gledenov, J. Andrzejweski, K. H. Guber, S. Raman, and T. Rauscher, Nucl. Phys. A **688**, 86c (2001).

[33] Yu. M. Gledenov, M. V. Sedysheva, V. A. Stolupin, Guohui Zhang, Jiaguo Zhang, Hao Wu, Jiaming Liu, Jinxiang Chen, G. Khuukhenkhuu, P. E. Koehler, and P. J. Szalanski, Phys. Rev. C **80**, 044602 (2009).

[34] I. Szarka, M. Florek, J. Oravec, and K. Holý, Nucl. Instrum. Methods Phys. Res. B **17**, 472 (1986).

[35] Yu. P. Popov, V. I. Salackij, and G. Khuukhenkhuu, Sov. J. Nucl. Phys. **32**, 459 (1980).

[36] A. Koning, S. Hilaire, and M. Duijvestijn, computer code TALYS, version 1.4, available online at http://www.talys.eu/ in *Proceedings of the International Conference on Nuclear Data for Science and Technology, April 22–27, Nice, France*, edited by O. Bersillon, F. Gunsing, E. Bauge, R. Jacmin, and S. Leray (EDP Sciences, Les Ulis Cedex A, France, 2008), pp. 211–214.

[37] T. Rauscher, computer code SMARAGD, http://www.nucastro.org/smaragd.html

[38] T. Rauscher, Astroph. J. Suppl. **201**, 26 (2012).

[39] T. Rauscher, http://www.nucastro.org